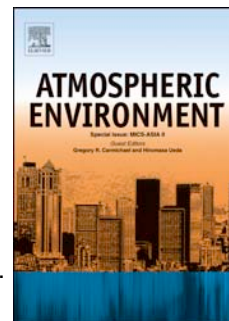# Accepted Manuscript

Influence of Wind Speed on Optical Properties of Aerosols in the Marine Boundary Layer Measured by Ship-Borne Depolarization Lidar in the Coastal Area of Korea

Dong Ho Shin, Detlef Müller, Taejin Choi, Young Min Noh, Young Jun Yoon, Kwon H. Lee, Sung Kyun Shin, Nam Yi Chae, Kwanchul Kim, Young J. Kim

Please cite this article as: Shin, D.H., Müller, D., Choi, T., Noh, Y.M., Yoon, Y.J., Lee, K.H., Shin, S.K., Chae, N.Y., Kim, K., Kim, Y.J., Influence of Wind Speed on Optical Properties of Aerosols in the Marine Boundary Layer Measured by Ship-Borne Depolarization Lidar in the Coastal Area of Korea, *Atmospheric Environment* (2013), doi: 10.1016/j.atmosenv.2013.10.027.

This is a PDF file of an unedited manuscript that has been accepted for publication. As a service to our customers we are providing this early version of the manuscript. The manuscript will undergo copyediting, typesetting, and review of the resulting proof before it is published in its final form. Please note that during the production process errors may be discovered which could affect the content, and all legal disclaimers that apply to the journal pertain.

1 **Influence of Wind Speed on Optical Properties of Aerosols in the**

2 **Marine Boundary Layer Measured by Ship-Borne Depolarization**

3 **Lidar in the Coastal Area of Korea**

4 Dong Ho Shin [a], Detlef Müller [b, c,] *, Taejin Choi [c], Young Min Noh [a], Young Jun Yoon [c],

5 Kwon H. Lee [e], Sung Kyun Shin [a], Nam Yi Chae [c], Kwanchul Kim[a], Young J. Kim[a]

6 [a] *School of Environmental Science & Engineering, Gwangju Institute of Science and Technology*

7 *(GIST) Oryong-dong, Buk-gu, Gwangju 500-712, Korea*

8 [b] *University of Hertfordshire, College Lane, Hatfield AL10 9AB, United Kingdom*

9 [c] *Science Systems and Applications, Inc., MS 475 NASA Langley Research Center, Hampton, VA*

10 *23681, USA*

11 [d] *Korea Polar Research Institute (KOPRI), Songdomirae-ro 26, Yeonsu-Gu, Incheon, Republic of*

12 *Korea*

13 [e] *Department of Satellite Geoinformatics Engineering, Kyungil Univ., Gyungsan 712-701, Rep. of*

14 *Korea*

15 [*] Corresponding Author

16 Detlef Mueller

17 Tel) +44 (0)1707 28 77803

18 Email) d.mueller@herts.ac.uk

19   **Abstract**

20   Shipboard measurements of microphysical and optical properties of marine boundary-layer

21   aerosols were performed around the Korean Peninsula from 2 to 5 December 2009. The

22   measurements were conducted aboard the Korean icebreaking research vessel Araon during

23   cruise tracks in the East Sea of Korea near Busan and Pohang. This paper describes the

24   results of optical aerosol measurements acquired with a DePolarization Lidar (DPL) and an

25   Optical Particle Counter (OPC) and data on meteorological parameters. Backward trajectory

26   analyses indicate that two different aerosol characteristics according to different pathways of

27   air mass encountered during the cruise. We find a high correlation between wind speeds

28   across the east coast of Korea and extinction coefficient, depolarization ratio and mass

29   concentration with correlation coefficient (R^2) of 0.57, 0.52 and 0.67, respectively. The

30   increase of extinction coefficient, depolarization ratio and number concentration with wind

31   speed may have been caused by the increase of sea-salt aerosol production and transport.

32   **Key words**; lidar; aerosol; wind speed; marine boundary layer

33   **1. Introduction**

34   Aerosols play a significant role in air quality and atmospheric visibility. They affect the

35   global climate because of their effect on the solar radiation. The so-called aerosol direct effect

36   occurs when aerosols affect the radiation budget by scattering and absorbing solar radiation

37   (Ayash et al., 2008; Ma et al., 2008). The aerosol indirect effect occurs when the optical

38   properties of clouds are changed, e.g. cloud condensation and lifetime processes, because of

39   the influence of microphysical and chemical characteristics of aerosol on cloud properties

40   (Goodale and Mansfield, 1987; Twomey et al., 1984).

41   The ocean is one of the major sources of natural aerosols. On the global scale, the total mass

42   of natural aerosols is much higher than that of anthropogenic aerosols. Sea salt is the

43   strongest natural source of aerosol with a production rate of about 1000 - 10,000 Tg per year

44   (Winter and Chýlek, 1997). Sea salt aerosols dominate the atmosphere clear-sky radiative

45   forcing over the oceans (Grini et al., 2002; Ma et al., 2008). Sea salt aerosols act as cloud

46   condensation nuclei (CCN) and modify the radiative properties and lifetime of clouds

47   (Murphy et al., 1998; Pierce and Adams, 2006). Therefore, changes in marine aerosol

48   properties are likely to have important climatological implications (Ayash et al., 2008;

49   Murphy et al., 1998).

50   The main mechanism leading to the production of sea salt aerosol is air bubbles bursting at

51   the surface of the ocean as a result of wind stress (An et al., 1986; Blanchard, 1983). The

52   bubbles are formed when breaking waves are lifted into the marine boundary layer (MBL)

53   (Blanchard and Syzdek, 1988). Breaking waves create whitecaps and sea-spray droplets that

54   consist of a large number of air bubbles, which is essential for the increased production of

55   marine aerosols (Fairall et al., 1983). As the bubbles fall back to the surface they form

56   whitecaps and burst, thus leading to the injection of sea water film and jet drops into the

57   atmosphere (Resch et al., 1986; Wu, 1990). A correlation was found between surface wind

58   speed and the aerosol concentration of sea salt (Latham and Smith, 1990; O'Dowd and Smith,

59   1993).

60   Despite their importance, marine aerosols remain one of the most poorly understood

61   aerosols in the atmosphere. Particularly, the relation between marine aerosol optical

62   properties and wind speed is difficult to quantify because it can be masked by the long-range

63   transport of aerosols that originate from land-based sources (Smirnov et al., 1995; Villevalde

64   et al., 1994) and get mixed into the marine boundary layer.

65   The main objective of this paper is to investigate the relationship between microphysical

66   and optical properties of marine aerosol along with their variation with wind speed. The

67   paper is organized as follows: Section 2 presents the method and the measurements. Section 3

68   discusses microphysical and optical properties of the marine aerosols observed in our study.

69   Section 4 summarizes our findings.

2. Measurement and Method

We used data from the ship-borne DePolarization Lidar (DPL), an Optical Particle Counter (OPC), and data obtained with hygrometer, thermometer, anemometer, and anemoscope. These instruments were installed aboard the research icebreaking Araon. Araon is operated by the Korea Polar Research Institute (KOPRI). The first cruise of Araon was mainly concentrated along the coast and lasted from 2 to 4 December 2009. Fig. 1 shows the cruise track of the Araon. We performed a backward trajectory analyses for aerosol transport characteristics. We identified air masses characteristic of clean marine conditions and air masses that were influenced by anthropogenic aerosols from East Asia.

2.1 DePolarization Lidar (DPL)

The DPL system is the first ship-borne lidar of Korea. The system was developed by KOPRI between March 2007 and April 2008. The lidar is installed on an optical table in a way that compensates for vibrations as much as possible. The lidar system is compact in size and it is installed in a container for deployments during cruises on Araon. The seatainer is weatherproof. A tilted, transparent glass roof protects the system against harsh environmental stress such as sea salt particles, exhaust from the Araon engine, ocean waves, precipitation, extreme humidity and temperature changes. The DPL system is operating without maintaining it each day. It can also be remote-controlled from other places through internet. The glass roof was cleaned by hand every few days and after rain during the campaign.

Fig. 2 shows the sketch of the DPL. The DPL system measures profiles of the linear depolarization ratio (DPR, δ) and backscatter coefficients of atmospheric particles at 532 nm wavelength. The light source of the lidar is a pulsed Nd:YAG laser (Quantel CFR400) which operates at the wavelength of 1064 nm. A frequency-doubling crystal allows for generating linear-polarized laser light at 532 nm wavelength. The laser emits pulses of 170 mJ at 532 nm wavelength. The pulse repetition rate is 30 Hz. The laser beam is transmitted vertically into the atmosphere after it is expanded five-fold. This system has a coaxial configuration

96   between the expanded laser beam and the receiver telescope. The backscattered light is

97   collected with an 8-inch Schmidt-Cassegrain telescope. After reflection from the secondary

98   mirror of the telescope, the backscattered light is focused to a pinhole. After passing the

99   pinhole, an achromatic lens collimates and transmits the light to an interference filter that

100 transmits at 532 nm. The interference filter is placed in front of a polarizing beam splitter

101 cube (PBC). The interference filter reduces the background noise from solar radiation. The

102 PBC is used to separate the parallel from the cross-polarized signals of the depolarized

103 backscatter signals. These two polarized beams then enter photomultiplier tubes (PMT)

104 which generate electronic signals which are subsequently collected by the data acquisition

105 system. The ratio of the gain of the two detectors was determined by rotating a half-

106 wavelength plate. The plate is located at the front end of the laser head. An analog-to-digital

107 converter (ADC) is used to digitize the output from the PMTs. The sampling rate is 60MHz.

108 Measurements were taken by collecting 3600 laser shots (2 minute time resolution) and a

109 vertical resolution of 2.5 m. The lowest height of complete overlap of laser beam and field of

110 view of the receiver telescope is 250 m.

111 The δ indicates if the scattering particles have non-spherical shape (Murayama et al., 2004;

112 Sassen, 1991). The volume DPR (δ_v) is defined as the ratio of the cross–polarized lidar return

113 signal with respect to the parallel-polarized backscatter signal (Freudenthaler et al., 2009;

114 Murayama et al., 1999; Sugimoto and Lee, 2006). The δ_v describes the sum of two

115 components, i.e., the molecular DPR (δ_m) and the particle DPR (δ_p). The δ_p can be defined by

116 the following equation:

117 $$\delta_p = (R\, \delta' - \delta_m)/(R - 1) \tag{1}$$

118 where $\delta' = \delta/(1 + \delta)$ (Murayama et al., 1999). The term R denotes the backscatter ratio. We

119 use a constant δ_m of 1.4 % (Cairo et al., 1999; Weber et al., 1967).

120 The uncertainty of δ_p comes from the error of the particle backscatter coefficient of the δ

121 calibration and systematic errors such as the incomplete separation of the linear polarization

122 due to the receiving optics (Cairo et al., 1999; Freudenthaler et al., 2009; Mattis et al., 2009).

123   Using the derived error formulas and estimations of the basic errors (Freudenthaler et al.,

124   2009), the δ_p values have a mean relative uncertainty of 15%.

125   The vertical optical profiles are derived on the basis of the Klett algorithm (Klett, 1985).

126   Before applying the Klett algorithm, we performed signal smoothing by Savitsky–Golay

127   filters for the random component of the error (Althausen et al., 2000; Whiteman, 1999).

128   Signal smoothing lengths are 50 m for backscatter coefficient and δ. Radiosondes were

129   launched two times a day (00:00 and 12:00 h, UTC) at Pohang (36.03° N, 129.38° E) which

130   is about 20-50 km away from the pathway of the research vessel. The Klett method needs as

131   input the lidar ratio and the reference value of the particle backscatter coefficient in a specific

132   height in order to derive the profile of the particle backscatter coefficient. The calibration

133   point of the backscatter profile of the raw signals was set in an altitude where no particles but

134   only molecules contributed to the measured signals.

135   The retrieval of the particle extinction coefficients from the elastic lidar signals significantly

136   depends on the correct choice of the lidar ratio. The lidar ratio is defined as the ratio of the

137   extinction coefficient to the backscatter coefficient. In general, the uncertainty of the profiles

138   of the extinction coefficient that are derived with this type of lidar are larger than the

139   uncertainty of the profiles of the backscatter coefficient. In that regard, we may use

140   information on so-called aerosol types which can be distinguished according to their lidar

141   ratio. We point out that the concept of using aerosol types can be used only as an

142   approximation in the data analysis. A clear distinction among aerosol types may only be

143   possible if these types occur in their pure form. Mixing of aerosol types, as it may easily

144   happen in East Asia washes out the clear separation. In our study we used the constant lidar

145   ratio of 23 sr (at 532 nm) for marine aerosols (Müller et al., 2007) . In view of the existing

146   literature we acknowledge the possibility that this value may not be characteristic for all types

147   of naturally occurring maritime aerosols. Furthermore, For calculation of backscatter

148   coefficient based on the 'Standard error propagation equation' (Bevington and Robinson,

149   1969), we consider signal noise and systematic errors (Ansmann et al., 1992; Gutkowicz-

150 Krusin, 1993). The relative statistical error of the backscatter coefficients is on the order of 5-

151 10% (Althausen et al., 2000; Noh et al., 2009; Tesche et al., 2009).

152 **2.2 Optical Particle Counter (OPC)**

153 Aerosol size distributions and number concentrations were measured with an OPC (Grimm

154 Model 265). The OPC was placed at the bottom of the radar master, 20 m above sea level.

155 The OPC detects scattered laser-light at a mean scattering angle of 90°. The serial binary

156 signals of the OPC were logged to a PC in the atmospheric lab room which was located on

157 the upper deck of the research vessel. The OPC provided 5-min averaged data of the number

158 size distribution binned into 31 different size ranges from 0.25 to 32 μm and above (all sizes

159 given as optically equivalent diameter). The OPC performed continuous sampling of the

160 aerosols from which the size distributions were determined and averaged for the

161 measurement times of the lidar observations. Mass concentrations were calculated from the

162 number size distributions (Burkart et al., 2010; Snider and Petters, 2008). The aerosol density

163 of 2.2 g/cm^3 for marine aerosol was used in the mass concentration calculation.(Fan and Toon,

164 2010; Tang et al., 1997). Data from the DPL and the OPC measurements were acquired

165 continuously during the cruise. The average time of the DPL and OPC was 10 and 5 minutes,

166 respectively. Measurement data contaminated by the ship exhaust plume were excluded from

167 the data analysis. For this purpose we used information on wind direction. The data were

168 retained when the relative wind direction was within 120° to the left and 60° to the right of

169 the ship heading. Wind directions and other meteorological data such as wind speed, air

170 temperature and relative humidity (RH) were measured at the top of radar mast at 20 m

171 height above sea level.

172   ## 3.   Result and Discussion

173   ### 3.1 Meteorological Conditions and Lidar Measurements

174   Fig. 3 shows the time series of the profiles of the DPL data and the meteorological data.

175   Fig. 3(a) and 3(b) show the time-height distributions of the range-corrected signals and the δ_m

176   acquired during the entire observation period. Because of precipitation caused by low-level

177   clouds, the lidar measurements were interrupted from 1250 UTC on 3 December to 0010

178   UTC on 4 December. Temporal variations of the backscatter coefficient and the δ_p at the

179   height of 300 ± 50 m are shown in Fig. 3(c). Note that calculation for the backscatter

180   coefficient and the δ_p was temporally interrupted from 1500 to 2400 UTC on December 2

181   and from 1250 UTC on 3 December to 0010 UTC on 4 December, because of the appearance

182   of clouds. Fig. 3(d) and 3(e) show the temporal variations of the meteorological parameters.

183   The total mass concentration of the aerosol particles is shown in Fig. 3(f). We categorized

184   period I and period II according to the air mass pathways that are shown in Fig. 3 (see section

185   3.2).

186   ### 3.2 Classification of the Atmospheric Conditions

187   Backward trajectory was analyzed to understand the air mass transport pathway and the

188   potential source regions encountered during the cruise. We analyzed the aerosol

189   characteristics with respect to categorized back trajectories for our initial estimation of the

190   sources of the aerosols. Four-days backward trajectories in the lower atmosphere were

191   calculated using the HYSPLIT (HYbrid Single-Particle Lagrangian Trajectory) model

192   (Draxler and Rolph, 2003; Rolph, 2003). Air mass backward trajectories that ended along the

193   cruise path were computed for heights of 300 m above sea level (see Fig. 4).

194   Period I denotes air masses that originated from the Chinese continent, passed across the

195   Korean Peninsula and then entered the measurement pathway across the line defined by

196   Busan, Pohang and Ulsan (these cities are the biggest harbor and industrial cities in Korea).

197   Period II denotes air masses that originated from the north of China and Siberia and entered

198   the measurement pathway along the east coast of the Korean Peninsula.

199   Fig. 4 (c) and (d) show the MODIS-retrieved AOD at 550 nm obtained by the modified

200   GSTAR algorithm (Lee et al., 2006a; Lee et al., 2006b) for 2 and 4 December 2009. Areas

201   where clouds or sun-glint was present or areas where there was an orbital gap in the data are

202   shown in white. The MODIS AOD over southeast coast of Korean peninsula (near the cruise

203   track of Araon; see Fig. 1) during period I shows higher values than the AOD that describes

204   period II.

3.3 Microphysical and Optical Properties

3.3.1 Vertical Profiles

207   Fig. 5(a) shows the vertical distributions of temperature, virtual potential temperature, and

208   RH obtained from radiosonde data. Fig. 5(b) shows calculated vertical profiles of aerosol

209   backscatter coefficients and the δ_p at 532 nm. The height of the MBL can be determined from

210   the vertical profiles of the aerosol backscatter coefficient (Drobinski et al., 1998), and the

211   base of inversion layer from the radiosonde data (Barnes et al., 1980; Zeng et al., 2010). The

212   region where the aerosol backscatter coefficient sharply decreases and the potential

213   temperature lapse rate changes can be used as an indicator of the top of the MBL. The slope

214   of the relative humidity profile and the virtual potential temperature profile sharply changes

215   between 1.3 and 1.7 km, which can also be used for identifying the top of the MBL. The

216   aerosol backscatter coefficient profiles show that the top of the MBL was at around 1.5 km

217   above sea level.

218   The height differences of the MBL that we obtain from the two methods can be caused by

219   different definitions that use different measurement parameters (Baars et al., 2008; Haeffelin

220 et al., 2012). The height of the MBL determined from the temperature profiles measured with

221 radiosonde was in good agreement to the MBL height determined from the aerosol profiles

222 measured with the DPL.

223 **3.3.2 Relationship Between Wind Speed and Aerosol Optical Properties**

224 Fig. 6 indicates a slight dependence of the δ_p with increasing wind speed. Regarding the

225 increase of the δ_p with increasing wind speed, the following causes are possible candidates:

226 (1) soil or dust particles transported from the continent, which can be seen from the back

227 trajectory analysis (see Fig. 4), may be mixed into the MBL; (2) sea-salt particles crystallize

228 by the strong sea breeze.

229 Soil and sea-salt particles are non-spherical and should increase the δ. Sea-salt particles are

230 hygroscopic. On the one hand, they do not markedly change their shape through uptake of

231 water until 75% RH is reached. On the other hand, humidified sea-salt particles can exist in a

232 supersaturated droplet phase until RH drops below 45–48% (Tang et al., 1977; Tang, 1996;

233 Winkler and Junge, 1971). In this study, during the two-measurement periods, RH was above

234 40% and below 75% which thus could have allowed for sea-salt particles being more in their

235 crystallized phase and/or more in their droplet phase.

236 We investigated the correlation of the aerosol extinction coefficient retrieved for the

237 altitude of 300 ± 50 m in dependence of the wind speed for the two measurement periods I

238 and II, respectively, see Fig. 7. We assume that the wind speeds at two different

239 measurement heights between extinction coefficient retrieval height at 300 ± 50 m and wind

240 speed measurement height at 20 m above sea level are almost equal in the MBL in view of

241 the small roughness lengths over water (Stull, 1988). We used the constant lidar ratio of 23

242 sr (at 532 nm) for marine aerosols. The following relationship holds for the data shown in

243 the scatter plots of Fig. 7:

244 $$\text{Period I:} \quad \alpha = 0.86 \times U + 17.02 \tag{2}$$

245 $$\text{Period II:} \quad \alpha = 1.32 \times U + 2.48 \tag{3}$$

246   where α is the extinction coefficient, and U is the wind speed. These equations explain that

247   the aerosol extinction coefficients increase with increasing wind speed. However, The air

248   mass pathway during period I has high chance to contain pollutions compared to period II air

249   mass because of different air mass origin and path way as shown in Fig. 4(a) and (b). These

250   differences induce the differences of constant which indicate background aerosol loading as

251   17.02 and 2.48 in Eq. (2) and (3), respectively. In that reason, the aerosol extinction

252   coefficients obtained during period I is higher than period II at the same or similar wind

253   speed. The scatter of the extinction coefficients in dependence of wind speed is considerably

254   smaller in period II compared to the scatter of data points that describe period I.

255   The slope between the aerosol extinction coefficient and wind speed of period II is about

256   1.5 times higher compared to the slope for period I. For period I we find an extinction

257   coefficient of ~15 Mm^{-1} for wind speed 0 m/s. In contrast, extinction coefficient seems to be

258   significantly lower for wind speed 0 m/s in period II. Though the regression line indicates a

259   value of 0 Mm^{-1}, we note that extinction coefficient seems to level out to a value of ~5–10

260   Mm^{-1} for wind speeds below ~5 m/s. The lack of data points below 5 m/s does not allow us to

261   make a clear conclusion on this point. We note, however, that this value of 5–10 Mm^{-1} would

262   result in an optical depth of 0.005–0.01 for a 1 km shallow, clean MBL and thus would

263   indicate background conditions. Such values have also been reported by Zielinski and Pflug

264   (2007) and Lehahn et al. (2010).

265   In the case of period I we find a high number concentration of aerosols compared to period

266   II (see Fig. 3(f), 4(c) and (d). The reason for this difference could be caused by the "purity"

267   of the marine aerosols in the sense that period I was characterized by the influence of

268   continental aerosols, see also the discussion given by Zielinski and Pflug (2007).

269   More work is required to further homogenize our data. In order to make sure that pure sea-

270   salt is responsible for the observed high DPRs and extinction coefficients at high wind speeds,

271   we need more filter samples and chemical analyses (Mayol-Bracero et al., 2002).

272   **3.3.3 Wind Speed Dependent Mass Concentration**

273   The OPC was used to investigate the relationship between aerosol concentration and wind

274   speed over the Korean coastal area. The generation mechanism of wind-driven sea-salt

275   particles is strongly related to wind speed (Blanchard and Woodcock, 2008; O'Dowd and

276   Smith, 1993). Mass concentrations of sea salt aerosols (C) are expressed by the following

277   equation (Kulkarni et al., 1982; O'Dowd et al., 1997; Wai and Tanner, 2004):

278
$$ln(C) = a \times U + b \qquad (4)$$

279   The term U is the wind speed, and "a" and "b" are constants. The constant "b" describes the

280   background sea-salt loading or the sea-salt concentration when wind speed reaches zero. This

281   equation implies that the sea salt concentrations are taken from air masses of pure marine

282   origin. Like in previous studies, we find a strong correlation between aerosol concentration

283   and wind speed during period II which describes the situation of a clean marine atmosphere

284   after a precipitation event, see the condition shown in Fig. 8.

285   According to equation (4) we obtain a log-linear dependence of the sea-salt concentration

286   with wind speed, i.e.,

287
$$ln(C) = 0.21 \times U + 2.23 \qquad (5)$$

288   The values of "a" and "b" from this work are within the range of values found from

289   previous studies, see Table 1 and Fig. 9. There are several reasons that may influence the

290   constants "a" and "b". (1) Different meteorology such as wind speed history, air/ sea

291   temperature, salinity and precipitation with geographic location will result in different

292   patterns for sea-salt generation and removal (Gong et al., 1997; Lovett, 1978). (2) The

293   measurement equipment and techniques that are used, such as the sampling time, measured

294   particle size ranges, altitude above sea level of the measurements and measurement sites

295   (Exton et al., 1985).

296   The value of slope "a" of our study is not significantly different from all other values

297   reported for "a" in previous studies; note the outlier reported by Tsunogai et al. (1972). In

298   contrast, the value ''b'' may vary across a rather wide range of numbers. The value we

299   obtained for ''b'' in our study is at the upper end of values reported in literature. The reason

300   for high value ''b'' is considered to be as follows: (1) We preformed measurement on a

301   moving ship, which may generate sea-salt particles (Lovett, 1978); (2) large particles which

302   contribute significantly to the sea salt concentration are easy to detected on the surface of the

303   ocean compared to inland measurement (Gong et al., 1997). Because residence time of the

304   larger sea salt particles is so short than small particles due to gravitational sedimentation

305   (Reid et al., 2001; Smith et al., 1993); (3) Sea-salt concentrations are higher in winter than

306   during the other seasons (Gong et al., 1997).

307   4.   Conclusion

308   Measurements of the optical properties of aerosols in the MBL were carried out along the

309   east coast of Korea during the Araon cruise. We used a DePolarization Lidar (DPL), an

310   optical particle counter (OPC) and meteorological instruments. The cruise was from 2 to 5

311   December 2009.

312   Different aerosol characteristics were observed and classified according to backward

313   trajectory analyses. The characteristics of aerosol microphysical and optical properties we

314   found during the measurement period are summarized as follows.

315   (1)   We identified two periods that are characterized by two different air mass types. Air

316   masses of period I originated from China and crossed the Korean Peninsula. Accordingly, the

317   air masses were influenced by pollution before they were advected out over the East Korean

318   coastline. In contrast, the air mass of period II passed along the east coast of Korea. In

319   addition this air mass was encountered after a precipitation event.

320   (2)   The lidar vertical profiles show that the backscatter coefficients increase with

321   decreasing height until the overlap region of the lidar is reached.

322   (3)   We reconfirm a log-linear variation of the aerosol number concentration versus wind

323 speed for Period II. In addition, we find that the particle depolarization ratio increases with

324 aerosol number concentration.

325   (4)   The aerosol extinction coefficients increase with increasing wind speed. A linear

326 relationship with a comparably high correlation coefficient is found for wind speed versus

327 particle depolarization ratio in period II.

328   We find different aerosol optical properties during the different periods, in period I, the

329 aerosols are composed of both natural and anthropogenic material. Aerosols of continental

330 origin may have been present in the marine boundary layer. In contrast, the aerosols of period

331 II were comprised mainly of particles of marine origin, i.e. sea salt particles.

332   In summary, further studies of the scattering properties of sea-salt aerosols under natural

333 conditions with known wind speeds are needed in order to estimate more precisely the net

334 global radiative forcing caused by these aerosol particles.

References

336 Althausen, D., Müller, D., Ansmann, A., Wandinger, U., Hube, H., Clauder, E., Zörner, S., 2000.
337 Scanning 6-wavelength 11-channel aerosol lidar. Journal of Atmospheric and Oceanic Technology 17,
338 1469-1482.

339 An, E., Spiel, D., Davidson, K., 1986. A model of marine aerosol generation via whitecaps and wave
340 disruption. Oceanic Whitecaps: And Their Role in Air-Sea Exchange Processes 2, 167.

341 Ansmann, A., Riebesell, M., Wandinger, U., Weitkamp, C., Voss, E., Lahmann, W., Michaelis, W.,
342 1992. Combined Raman elastic-backscatter lidar for vertical profiling of moisture, aerosol extinction,
343 backscatter, and lidar ratio. Applied Physics B 55, 18-28.

344 Ayash, T., Gong, S., Jia, C.Q., 2008. Direct and indirect shortwave radiative effects of sea salt
345 aerosols. Journal of Climate 21, 3207-3220.

346 Baars, H., Ansmann, A., Engelmann, R., Althausen, D., 2008. Continuous monitoring of the boundary-
347 layer top with lidar. Atmos. Chem. Phys 8, 7281-7296.

348 Barnes, G., Emmitt, G.D., Brummer, B., LeMone, M.A., Nicholls, S., 1980. The structure of a fair
349 weather boundary layer based on the result of several measurement strategies. Monthly Weather
350 Review 108, 349-364.

351 Bevington, P.R., Robinson, D.K., 1969. Data reduction and error analysis for the physical sciences.
352 McGraw-Hill New York.

353 Blanchard, D., 1983. The production, distribution, and bacterial enrichment of the sea-salt aerosol.
354 Air-sea exchange of gases and particles, 407-454.

355 Blanchard, D.C., Syzdek, L.D., 1988. Film drop production as a function of bubble size. Journal of
356 geophysical research 93, 3649-3654.

357 Blanchard, D.C., Woodcock, A.H., 2008. THE PRODUCTION, CONCENTRATION, AND VERTICAL

358 DISTRIBUTION OF THE SEA-SALT AEROSOL*. Annals of the New York Academy of Sciences 338,

359 330-347.

360 Burkart, J., Steiner, G., Reischl, G., Moshammer, H., Neuberger, M., Hitzenberger, R., 2010.
361 Characterizing the performance of two optical particle counters (Grimm OPC1. 108 and OPC1. 109)
362 under urban aerosol conditions. Journal of Aerosol Science 41, 953-962.

363 Cairo, F., Di Donfrancesco, G., Adriani, A., Pulvirenti, L., Fierli, F., 1999. Comparison of various linear
364 depolarization parameters measured by lidar. Applied Optics 38, 4425-4432.

365 Draxler, R., Rolph, G., 2003. HYSPLIT (HYbrid Single-Particle Lagrangian Integrated Trajectory)
366 model access via NOAA ARL READY website (http://www. arl. noaa. gov/ready/hysplit4. html). NOAA
367 Air Resources Laboratory, Silver Spring. Md.

368 Drobinski, P., Brown, R., Flamant, P.H., Pelon, J., 1998. Evidence of organized large eddies by
369 ground-based Doppler lidar, sonic anemometer and sodar. Boundary-Layer Meteorology 88, 343-361.

370 Exton, H., Latham, J., Park, P., Perry, S., Smith, M., Allan, R., 1985. The production and dispersal of
371 marine aerosol. Quarterly Journal of the Royal Meteorological Society 111, 817-837.

372 Fairall, C., Davidson, K., Schacher, G., 1983. An analysis of the surface production of sea-salt

373 aerosols. Tellus B 35, 31-39.

374 Fan, T., Toon, O., 2010. Modeling sea-salt aerosol in a coupled climate and sectional microphysical
375 model: mass, optical depth and number concentration. Atmospheric Chemistry and Physics
376 Discussions 10, 24499-24561.

377 Freudenthaler, V., Esselborn, M., Wiegner, M., Heese, B., Tesche, M., Ansmann, A., Müller, D.,
378 Althausen, D., Wirth, M., Fix, A., 2009. Depolarization ratio profiling at several wavelengths in pure
379 Saharan dust during SAMUM 2006. Tellus B 61, 165-179.

380 Gong, S., Barrie, L., Blanchet, J., 1997. Modeling sea-salt aerosols in the atmosphere 1. Model
381 development. JOURNAL OF GEOPHYSICAL RESEARCH-ALL SERIES- 102, 3805-3818.

382 Goodale, M., Mansfield, R., 1987. Climate Forcing by Antlropogenic Aerosols. Neuropsychologia 25,
383 97.

384 Grini, A., Myhre, G., Sundet, J.K., Isaksen, I.S.A., 2002. Modeling the annual cycle of sea salt in the
385 global 3D model Oslo CTM2: Concentrations, fluxes, and radiative impact. Journal of Climate 15,
386 1717-1730.

387 Gutkowicz-Krusin, D., 1993. Multiangle lidar performance in the presence of horizontal
388 inhomogeneities in atmospheric extinction and scattering. Applied Optics 32, 3266-3272.

389 Haeffelin, M., Angelini, F., Morille, Y., Martucci, G., Frey, S., Gobbi, G., Lolli, S., O'Dowd, C., Sauvage,
390 L., Xueref-Rémy, I., 2012. Evaluation of mixing-height retrievals from automatic profiling lidars and
391 ceilometers in view of future integrated networks in Europe. Boundary-Layer Meteorology 143, 49-75.

392 Klett, J.D., 1985. Lidar inversion with variable backscatter/extinction ratios. Applied Optics 24, 1638-
393 1643.

394 Kulkarni, M., Adiga, B., Kapoor, R., Shirvaikar, V., 1982. Sea Salt in Coastal Air and its Deposition on
395 Porcelain Insulators. Journal of Applied Meteorology 21, 350-355.

396 Latham, J., Smith, M., 1990. Effect on global warming of wind-dependent aerosol generation at the
397 ocean surface.

398 Lee, K.H., Kim, Y.J., Kim, M.J., 2006a. Characteristics of aerosol observed during two severe haze
399 events over Korea in June and October 2004. Atmospheric Environment 40, 5146-5155.

400 Lee, K.H., Kim, Y.J., Von Hoyningen-Huene, W., Burlow, J.P., 2006b. Influence of land surface effects

401 on MODIS aerosol retrieval using the BAER method over Korea. International Journal of Remote
402 Sensing 27, 5125-5125.

403 Lehahn, Y., Koren, I., Boss, E., Ben-Ami, Y., Altaratz, O., 2010. Estimating the maritime component of
404 aerosol optical depth and its dependency on surface wind speed using satellite data. Atmos. Chem.
405 Phys 10, 6711-6720.

406 Lovett, R., 1978. Quantitative measurement of airborne sea-salt in the North Atlantic. Tellus 30, 358-

407 364.

408 Müller, D., Ansmann, A., Mattis, I., Tesche, M., Wandinger, U., Althausen, D., Pisani, G., 2007.
409 Aerosol-type-dependent lidar ratios observed with Raman lidar. Journal of geophysical research 112,
410 D16202.

411 Ma, X., Von Salzen, K., Li, J., 2008. Modelling sea salt aerosol and its direct and indirect effects on
412 climate. Atmospheric Chemistry and Physics 8, 1311-1327.

413 Mattis, I., Tesche, M., Grein, M., Freudenthaler, V., Müller, D., 2009. Systematic error of lidar profiles
414 caused by a polarization-dependent receiver transmission: Quantification and error correction scheme.
415 Applied Optics 48, 2742-2751.

416 Mayol-Bracero, O., Gabriel, R., Andreae, M., Kirchstetter, T., Novakov, T., Ogren, J., Sheridan, P.,
417 Streets, D., 2002. Carbonaceous aerosols over the Indian Ocean during the Indian Ocean Experiment
418 (INDOEX): Chemical characterization, optical properties, and probable sources. Journal of
419 geophysical research 107, 8030.

420 Murayama, T., Müller, D., Wada, K., Shimizu, A., Sekiguchi, M., Tsukamoto, T., 2004.

421 Characterization of Asian dust and Siberian smoke with multi-wavelength Raman lidar over Tokyo,

422 Japan in spring 2003. Geophysical Research Letters 31, L23103.

423 Murayama, T., Okamoto, H., Kaneyasu, N., Kamataki, H., Miura, K., 1999. Application of lidar

424 depolarization measurement in the atmospheric boundary layer: Effects of dust and sea-salt particles.

425 Journal of geophysical research 104, 31.

426 Murphy, D., Anderson, J., Quinn, P., McInnes, L., Brechtel, F., Kreidenweis, S., Middlebrook, A.,

427 Posfai, M., Thomson, D., Buseck, P., 1998. Influence of sea-salt on aerosol radiative properties in the

428 Southern Ocean marine boundary layer. Nature 392, 62-65.

429 Noh, Y.M., Müller, D., Shin, D.H., Lee, H., Jung, J.S., Lee, K.H., Cribb, M., Li, Z., Kim, Y.J., 2009.

430 Optical and microphysical properties of severe haze and smoke aerosol measured by integrated

431 remote sensing techniques in Gwangju, Korea. Atmospheric Environment 43, 879-888.

432 O'Dowd, C.D., Smith, M.H., 1993. Physicochemical properties of aerosols over the northeast Atlantic:

433 Evidence for wind-speed-related submicron sea-salt aerosol production. Journal of geophysical

434 research 98, 1137-1149.

435 O'Dowd, C.D., Smith, M.H., Consterdine, I.E., Lowe, J.A., 1997. Marine aerosol, sea-salt, and the

436 marine sulphur cycle: A short review. Atmospheric Environment 31, 73-80.

437 Pierce, J.R., Adams, P.J., 2006. Global evaluation of CCN formation by direct emission of sea salt

438 and growth of ultrafine sea salt. Journal of geophysical research 111, D06203.

439 Reid, J.S., Jonsson, H.H., Smith, M.H., Smirnov, A., 2001. Evolution of the vertical profile and flux of

440 large sea-salt particles in a coastal zone. Journal of Geophysical Research: Atmospheres (1984–

441 2012) 106, 12039-12053.

442 Resch, F., Darrozes, J., Afeti, G., 1986. Marine liquid aerosol production from bursting of air bubbles.

443 Journal of geophysical research 91, 1019-1029.

444 Rolph, G., 2003. Real-time Environmental Applications and Display sYstem (READY) Website

445 (http://www. arl. noaa. gov/ready/hysplit4. html). NOAA Air Resources Laboratory, Silver Spring. MD.

446 Sassen, K., 1991. The polarization lidar technique for cloud research: A review and current

447 assessment. Bulletin of the American Meteorological Society 72, 1848-1866.

448 Smirnov, A., Villevalde, Y., O'Neill, N., Royer, A., Tarussov, A., 1995. Aerosol optical depth over the

449 oceans: Analysis in terms of synoptic air mass types. JOURNAL OF GEOPHYSICAL RESEARCH-

450 ALL SERIES- 100, 16-16.

451 Smith, M., Park, P., Consterdine, I., 1993. Marine aerosol concentrations and estimated fluxes over

452 the sea. Quarterly Journal of the Royal Meteorological Society 119, 809-824.

453 Snider, J.R., Petters, M.D., 2008. Optical particle counter measurement of marine aerosol

454 hygroscopic growth. Atmos. Chem. Phys 8, 1949-1962.

455 Stull, R.B., 1988. An introduction to boundary layer meteorology. Springer.

456 Sugimoto, N., Lee, C.H., 2006. Characteristics of dust aerosols inferred from lidar depolarization
457 measurements at two wavelengths. Applied Optics 45, 7468-7474.
458 Tang, I., Munkelwitz, H., Davis, J., 1977. Aerosol growth studies—II. Preparation and growth
459 measurements of monodisperse salt aerosols. Journal of Aerosol Science 8, 149-159.
460 Tang, I.N., 1996. Chemical and size effects of hygroscopic aerosols on light scattering coefficients.
461 JOURNAL OF GEOPHYSICAL RESEARCH-ALL SERIES- 101, 19-19.
462 Tang, I.N., Tridico, A., Fung, K., 1997. Thermodynamic and optical properties of sea salt aerosols.
463 Journal of Geophysical Research: Atmospheres (1984–2012) 102, 23269-23275.
464 Tesche, M., Ansmann, A., Müller, D., Althausen, D., Mattis, I., Heese, B., Freudenthaler, V., Wiegner,
465 M., Esselborn, M., Pisani, G., 2009. Vertical profiling of Saharan dust with Raman lidars and airborne
466 HSRL in southern Morocco during SAMUM. Tellus B 61, 144-164.
467 Tsunogai, S., Saito, O., Yamada, K., Nakaya, S., 1972. Chemical composition of oceanic aerosol.
468 Journal of geophysical research 77, 5283-5292.
469 Twomey, S.A., Piepgrass, M., Wolfe, T., 1984. An assessment of the impact of pollution on global
470 cloud albedo. Tellus B 36, 356-366.
471 Villevalde, Y.V., Smirnov, A., O'neill, N., Smyshlyaev, S., Yakovlev, V., 1994. Measurement of aerosol
472 optical depth in the Pacific Ocean and the North Atlantic. Journal of geophysical research 99, 20983-
473 20920,20988.
474 Wai, K.M., Tanner, P.A., 2004. Wind-dependent sea salt aerosol in a Western Pacific coastal area.
475 Atmospheric Environment 38, 1167-1171.
476 Weber, A., Porto, S.P.S., Cheesman, L.E., Barrett, J.J., 1967. High-resolution Raman spectroscopy of
477 gases with cw-laser excitation. JOSA 57, 19-27.
478 Whiteman, D.N., 1999. Application of statistical methods to the determination of slope in lidar data.
479 Applied Optics 38, 3360-3369.
480 Winkler, P., Junge, C.E., 1971. CommentsAnomalous Deliquescence of Sea Spray Aerosols'. Journal
481 of Applied Meteorology 10, 160-163.

482 Winter, B., Chýlek, P., 1997. Contribution of sea salt aerosol to the planetary clear-sky albedo. Tellus

483 B 49, 72-79.
484 Wu, J., 1990. Comment on "Film drop production as a function of bubble size" by DC Blanchard and
485 LD Syzdek. Journal of geophysical research 95, 7389-7391.
486 Zeng, X., Brunke, M.A., Zhou, M., Fairall, C., Bond, N.A., Lenschow, D.H., 2010. Marine atmospheric
487 boundary layer height over the eastern Pacific: Data analysis and model evaluation.
488 Zielinski, T., Pflug, B., 2007. Lidar-based studies of aerosol optical properties over coastal areas.
489 Sensors 7, 3347-3365.

490

491

492

493

494

495

496

497

498

499

500

501

502 **Fig. 1.** Cruise track of Araon. The blue numbers Julian day in 2009 denote the position of the
503   vessel.

504 **Fig. 2.** Schematic layout of the lidar system.

505 **Fig. 3.** Temporal changes of the lidar data and the sea surface meteorological data taken
506   between 0000 UTC on 2 December and 1200 UTC on 4 December 2009. We show
507   (a) vertical profiles of the range corrected backscatter signal, (b) the δ_v, (c) the
508   temporal changes of the δ_p and the backscatter coefficients at 300 ± 50 m above sea
509   level, (d) temperature (Black line) and relative humidity (Blue line), (e) wind speed
510   and direction, and (f) PM2.5 and PM10 concentrations. Periods I and II are
511   identified on the basis of backward trajectory analysis, as discussed in section 3.2.
512   The gap in the data in Fig. 3(a), (b), (c) and (f) indicate the missing data period
513   caused by precipitation.

514 **Fig. 4.** Four-day backward trajectory of air masses computed with the NOAA/ARL
515   HYSPLIT model for (a) the measurement period I and (b) the measurement period II.
516   Each line represents backward trajectories of two-hour time intervals arriving along
517   the cruise track at 300 m above sea level. The MODIS-derived spatial distribution of
518   aerosol optical depth in (c) on 2 December (period I) and (d) 4 December (period II)
519   is shown, too.

520 **Fig. 5**. DPL analysis and radiosonde results obtained (a) and (b) on 2 December 2009, 1200
521   UTC (Period I), and (c) and (d) 4 December 2009, 0000 UTC (Period II). We show
522   backscatter coefficients and $\boldsymbol{\delta_p}$s based on DPL measurements at 532 nm (b) and (d),
523   and temperature T, virtual potential temperature Θ_v, dew point T_d, and relative
524   humidity RH values measured by radiosonde (a) and (c). The error bars indicate
525   15% error for the backscatter profiles and for the δ_p.

526   **Fig. 6.** Variations of the δ_p (532 nm) at 300 ± 50 m height above sea level in dependence of
527   wind speed (U). The open blue circles describe period I; the open red squares
528   describe period II. The bold lines illustrate the linear regression lines of the two
529   periods. The error bars indicate an error of 15% for the δ_p. N and R^2 are the number
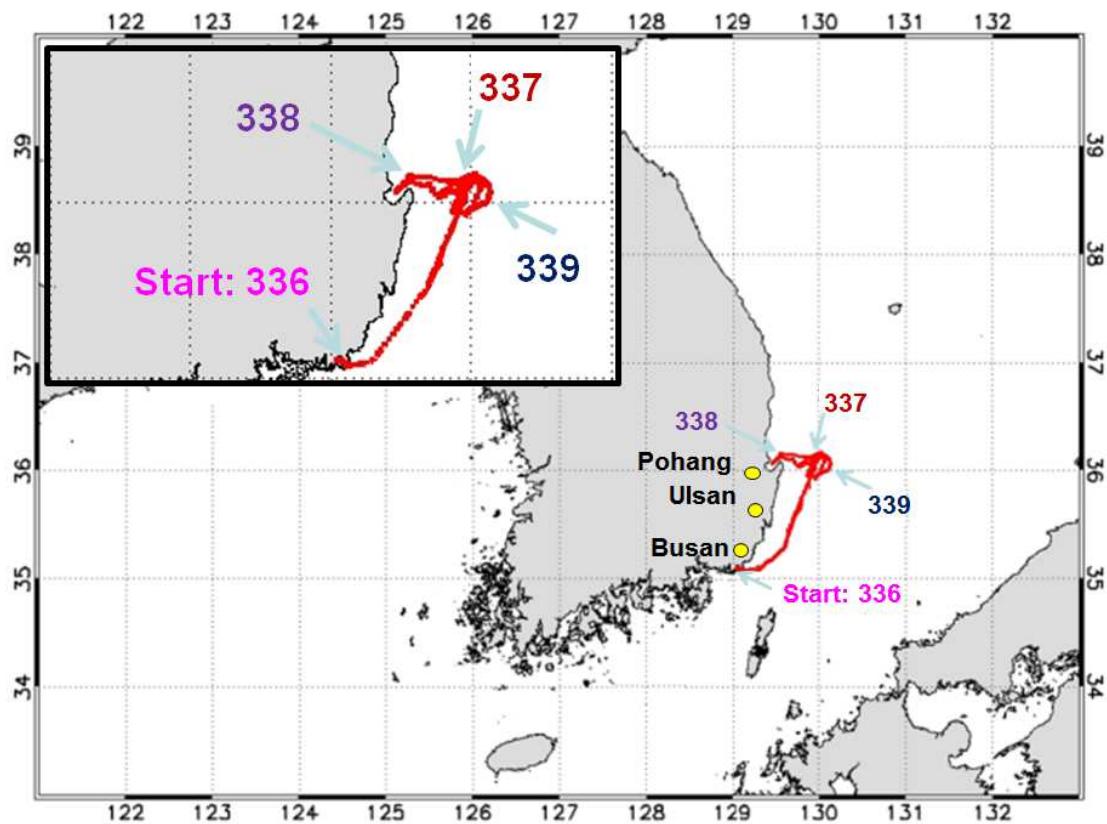530   of measurement points and the correlation coefficients, respectively.

531   **Fig. 7.** Dependence of the extinction coefficient (532 nm) at 300 ± 50 m height above sea
532   level versus surface wind speed. The bold black line illustrates the linear regression;
533   the equation and correlation coefficients (R) for the regressions are also shown.

534   **Fig. 8**. Scatter plot of the PM10 concentration ($\mu g/m^3$) on a logarithmic scale versus wind
535   speed (m/s) of period II.

536   **Fig. 9.** Comparison of sea-salt mass concentration as a function of wind speed and location of
537   measurement site.

538   **Table 1.** Values of a, b in Eq. (1) obtained from previous studies

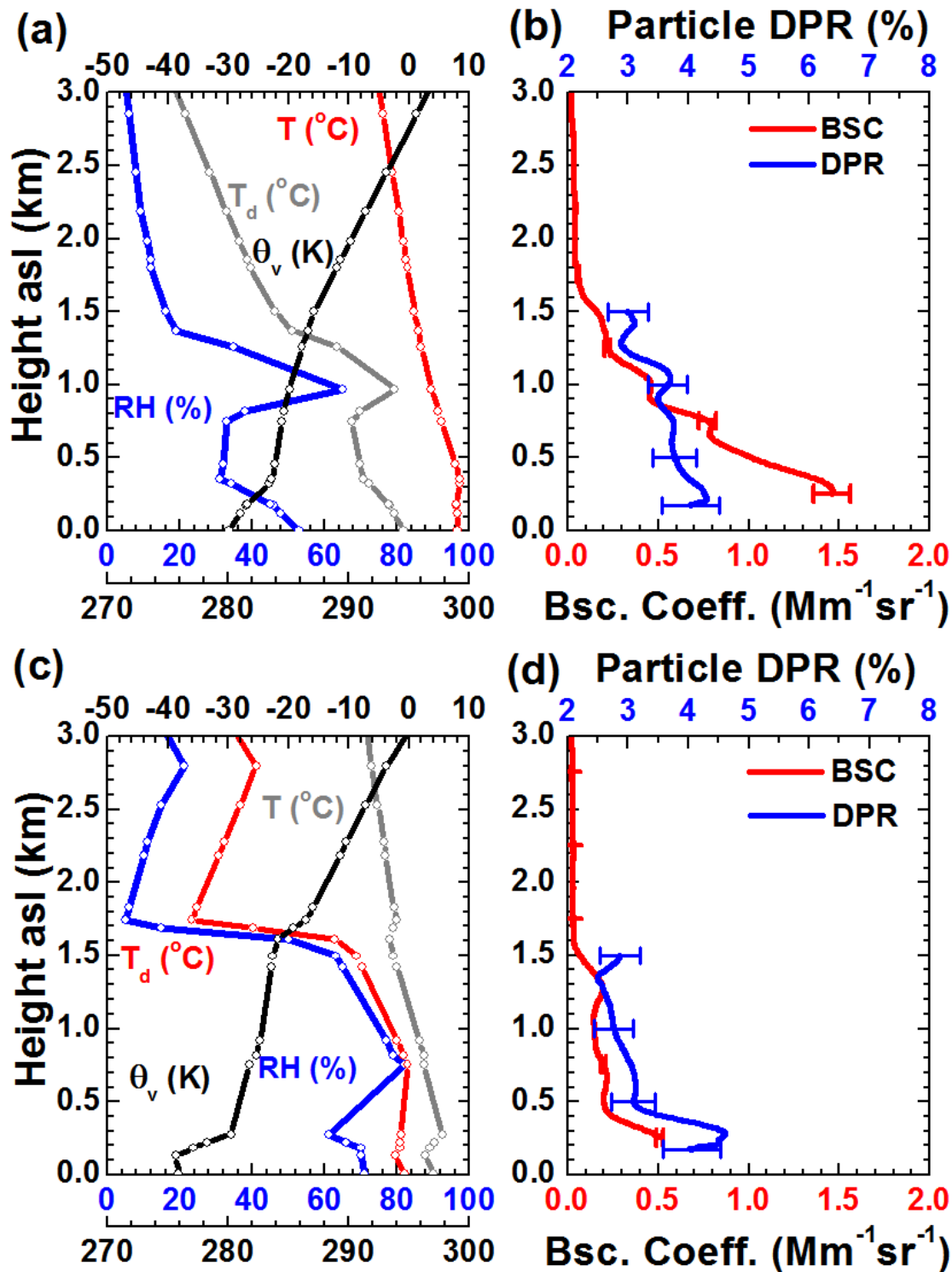| a (s/m)	b, (μg/m³)	sampling height	Region	Measurement time	Reference
0.16	2.57	600 m	Cloud base over Pacific Ocean	1952	Woodcock, 1953
0.16	13.3	15 m	The island of South Uist in the Outer Hebrides North Sea, on Platform	1980/1983	Exton et al., 1985
0.16	4.26	5–15 m	Atlantic Ocean, on ship	September 1974 to July 1975	Lovett, 1978
0.23	1.13	12 m	Noordwijk in the North Sea, on the research platform (51° S, 4° E)	October-November1986	Marks, 1990
0.21	9.23	20m	East sea of Korea (36° N, 129° E)	Dec-09	This study
0.27	5.35	1.2 m	1.8km inland of Western Indian coast	June-September 1977 and June-August 1978	Kulkarni et al., 1982
0.17	0.64	77 m;	Central Western (residential, location 22.1° N, 114.8° E)		Wai and Tanner, 2004
0.13	0.87	16 m	Sham Shui Po (mixed residential, commercial, industrial, 22.2° N, 114.9° E)	1995–1999	Tsunogai et al., 1972
0.19	0.45	24 m	Yuen Long (residential with fairly rapid urban development, 22.2° N, 114. 1° E)		Gras and Ayers, 1983
0.62	0.33	12–14 m	Pacific Ocean	May, 1964	Exton et al., 1985
0.12	2.52	94 m	Cape Grim, Tasmaniat Cape Grim (41° S, 145° E)	February 1978 to May 1980	Lovett, 1978

Figure showing Particle DPR (%) versus Wind Speed (m/s) with legend:
- Period I: $\delta_p = 0.10 \times U + 2.89$, ($R^2 = 0.25$, N=136)
- Period II: $\delta_p = 0.23 \times U + 1.87$, ($R^2 = 0.52$, N=64)
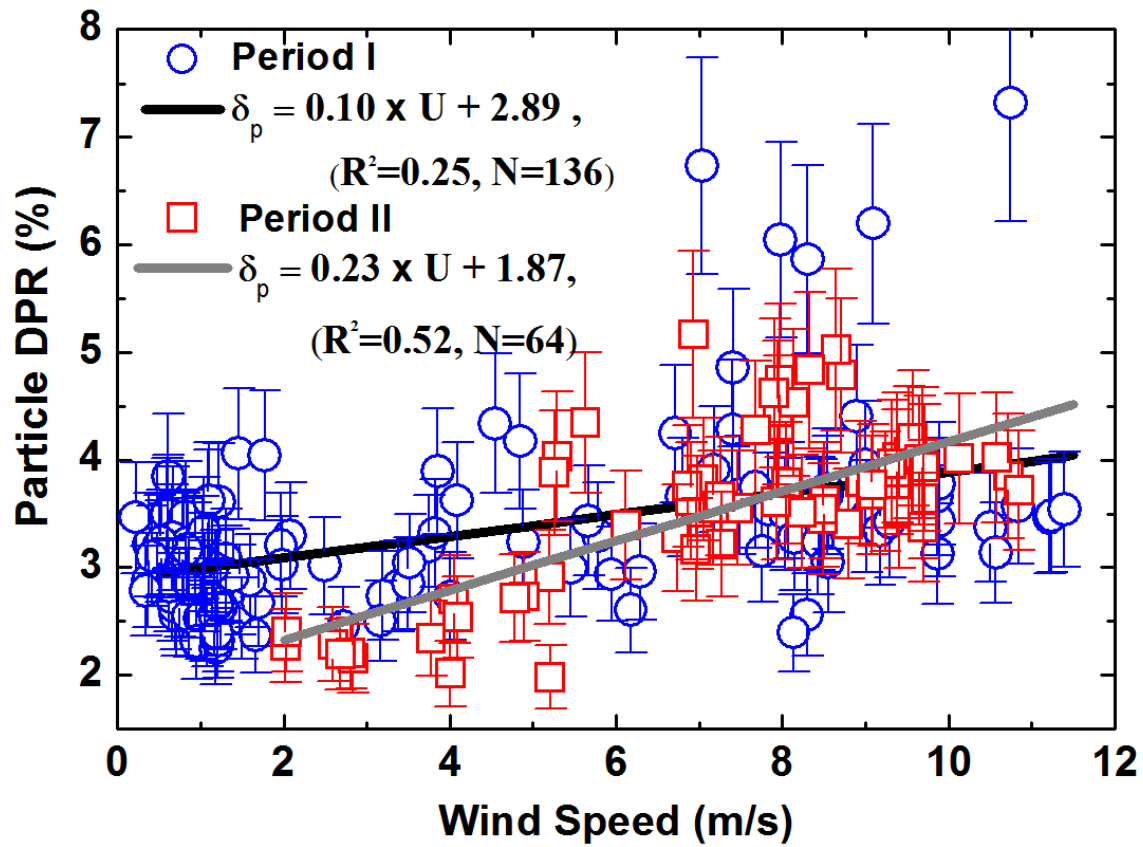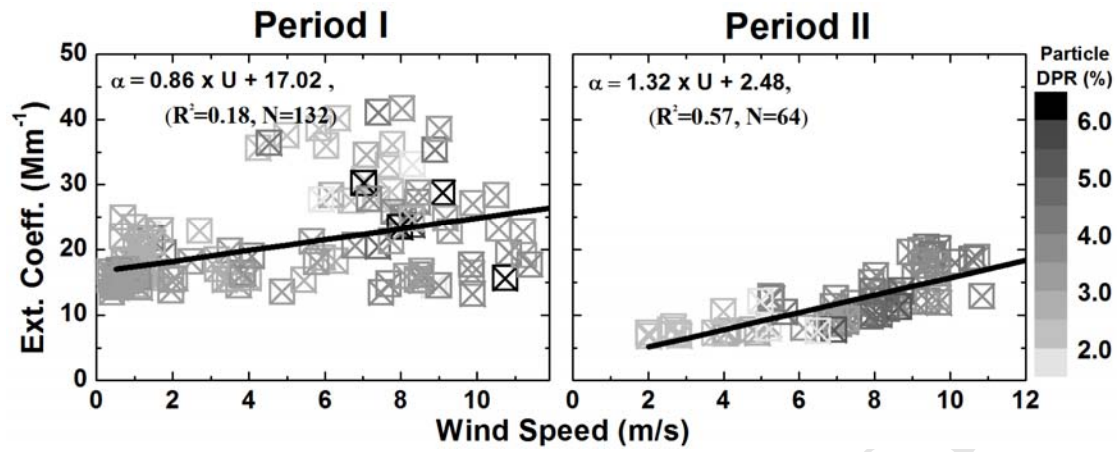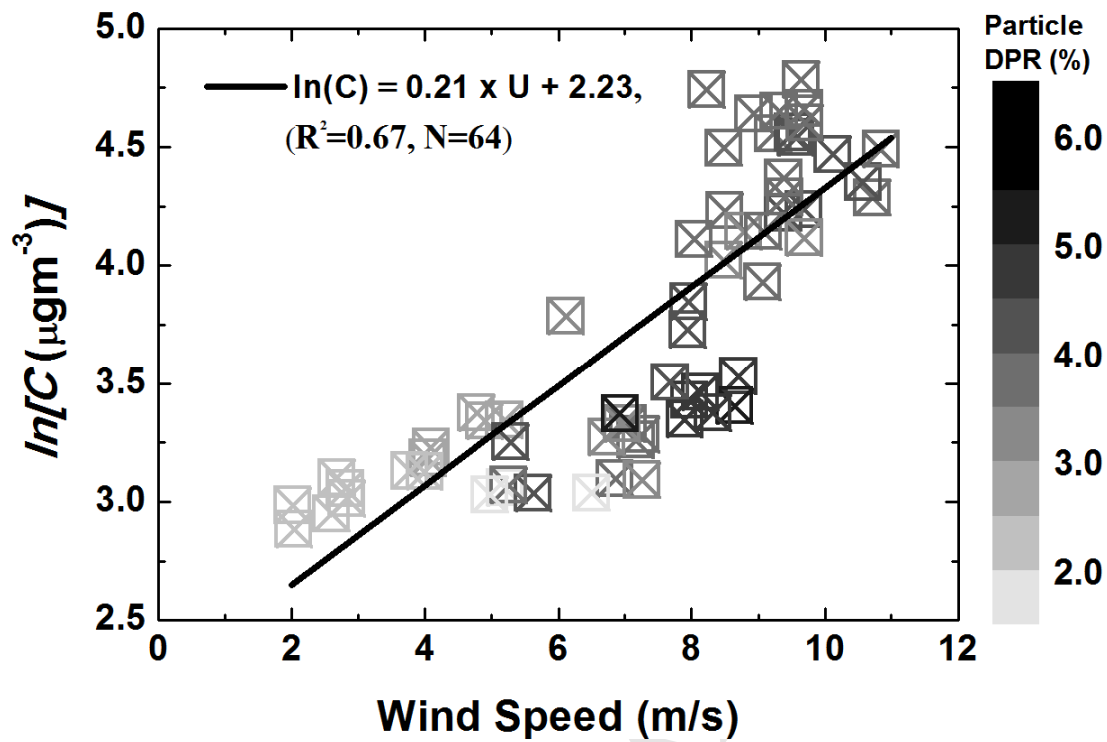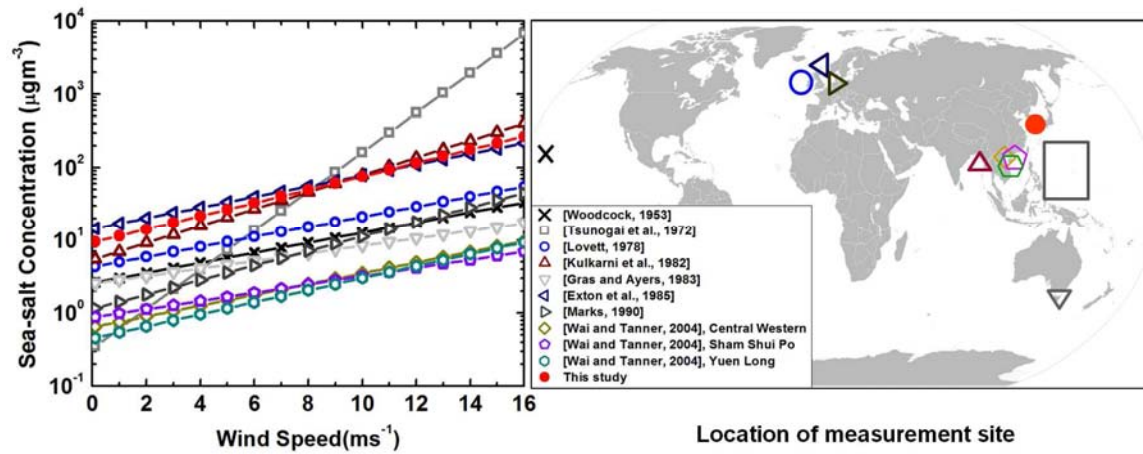
Location of measurement site
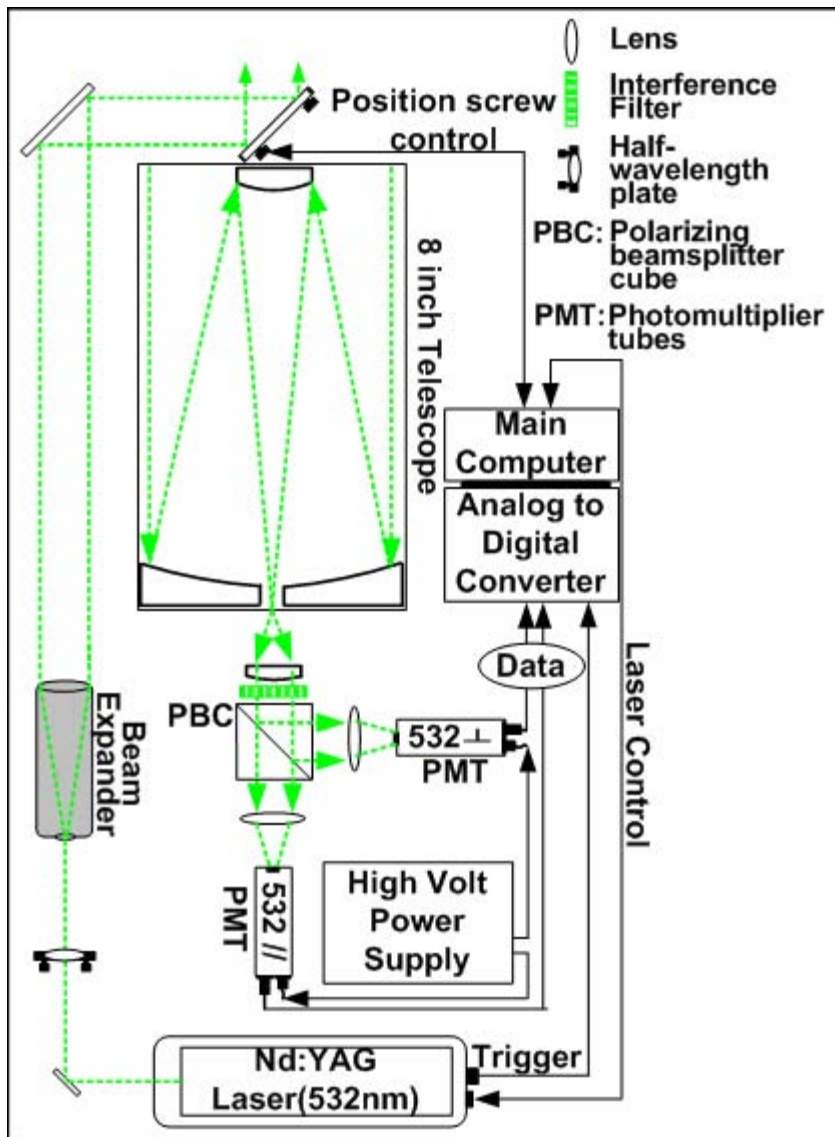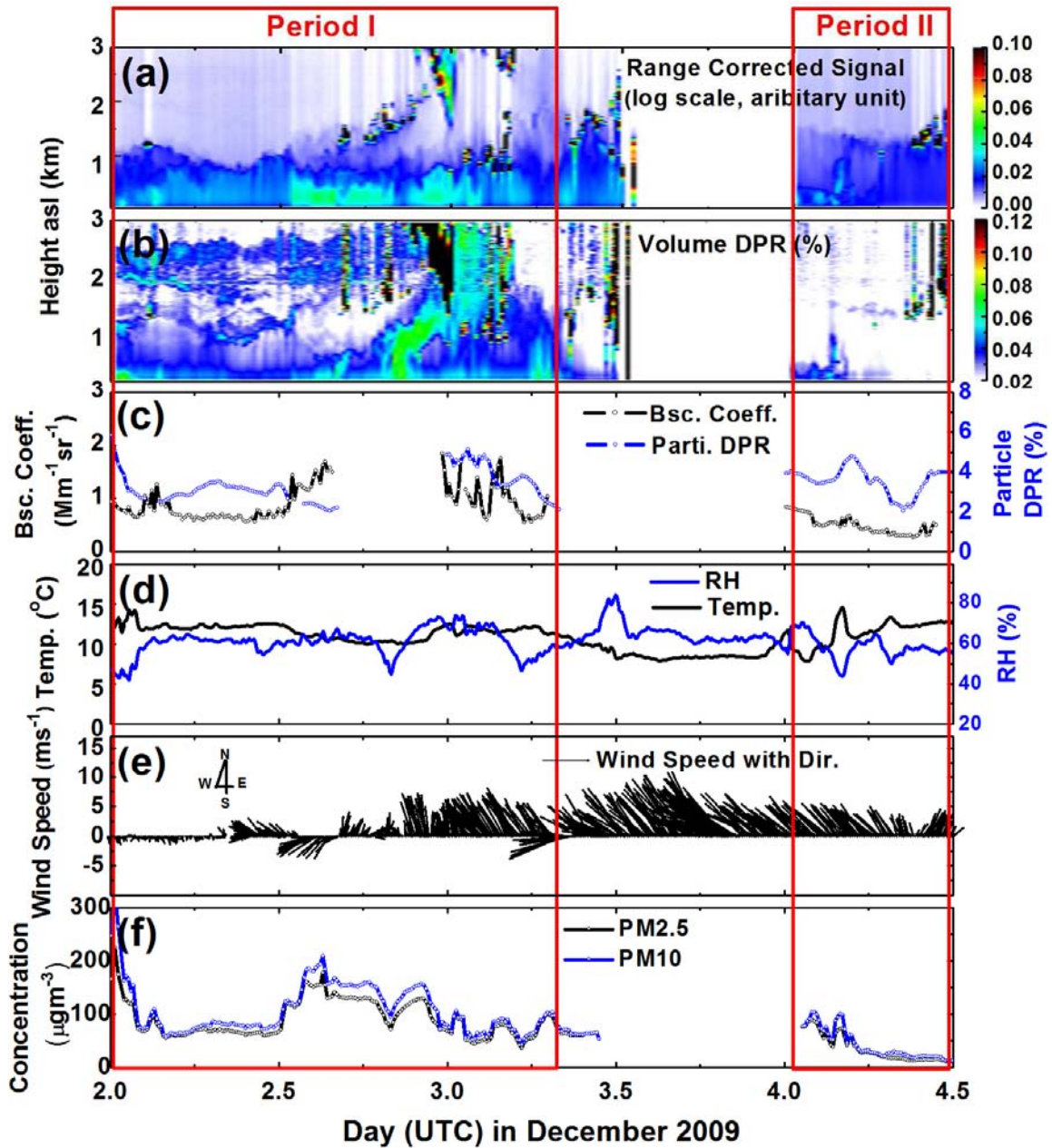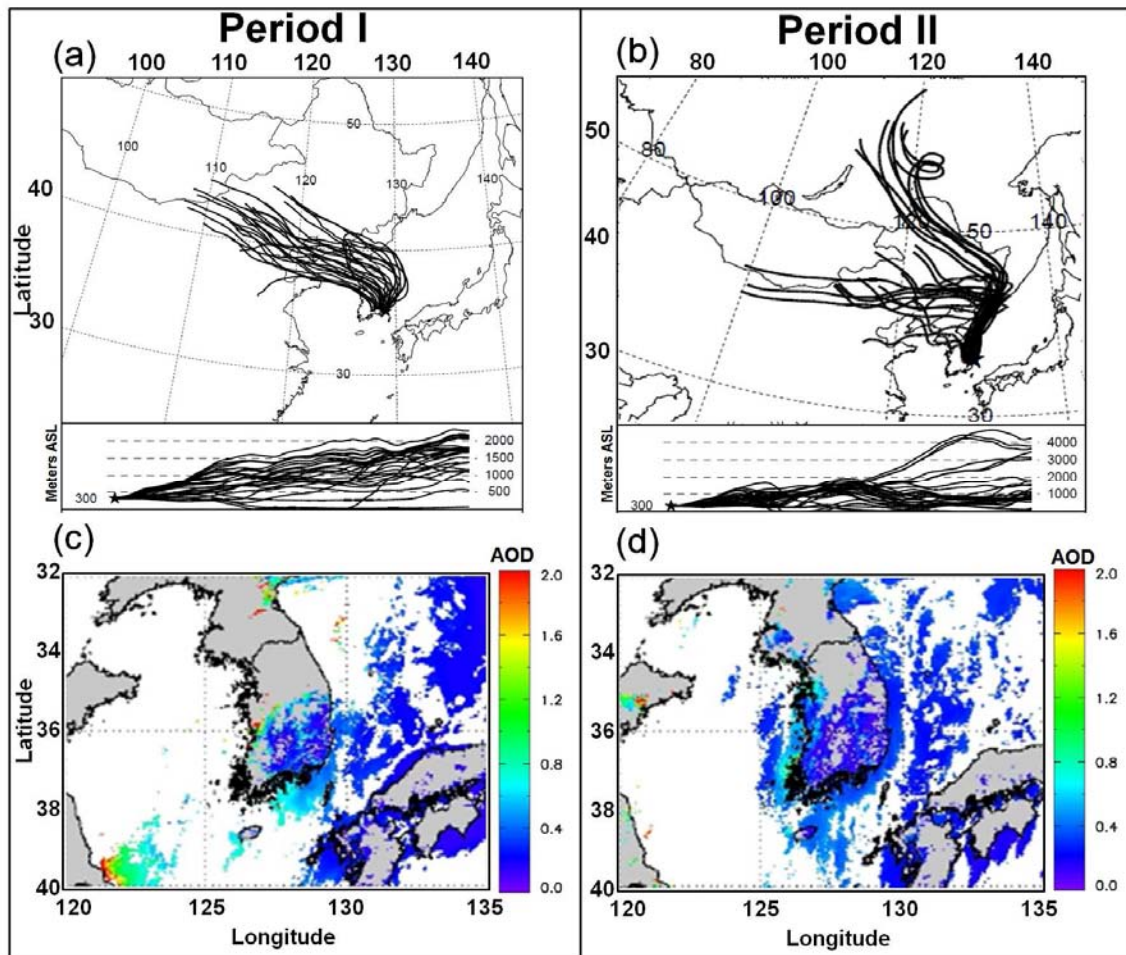
- Shipborne depolarization aerosol lidar measurements near Korean peninsula.

- Characterization of sea-salt particles with lidar in the eastern Pacific region.

- Correlation of sea-salt optical properties with wind speed provides parameterization.

- Correlation may be caused by with duration of transport over the ocean, too.

- Our results are comparable to correlation parameters reported in literature.